

# Chapter 7

## In Situ and Ex Situ Spectrophotometric Characterization of Single- and Multilayer-Coatings I: Basics

Olaf Stenzel and Steffen Wilbrandt

**Abstract** Optical spectrophotometry provides a powerful tool for the characterization of modern coatings, no matter whether they are manufactured for optical or non-optical applications. Spectrophotometry of coatings gives primary access to optical constants and their dispersion as well as to the film thickness. In a second step, the application of sophisticated Kramers–Kronig-consistent dispersion models gives further access to related quantities, including density, porosity, but also charge carrier density, crystalline structure, band structure and possible impurities of the coating. We will present and discuss the state of the art in spectrophotometry of single and multilayer coatings, including their in situ as well as ex situ versions. In situ spectrophotometry allows re-engineering as well as monitoring the deposition process of a growing coating, resulting in excellent specification adherence particularly in the field of optical coatings.

### 7.1 Introduction

The present chapter deals with the application of spectrophotometry for characterization of thin (solid) films. The general idea of spectrophotometric characterization

---

O. Stenzel (✉) · S. Wilbrandt

Fraunhofer Institute for Applied Optics and Precision Engineering IOF, Albert-Einstein-Str. 7,  
07745 Jena, Germany

e-mail: olaf.stenzel@iof.fraunhofer.de; optikbuch@optimon.de

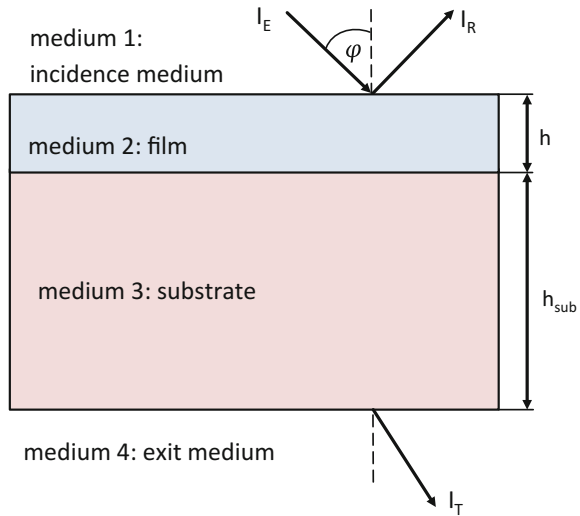
S. Wilbrandt

e-mail: steffen.wilbrandt@iof.fraunhofer.de

O. Stenzel

Abbe School of Photonics, Friedrich-Schiller-University Jena, Albert-Einstein-Straße 6, 07745  
Jena, Germany

**Fig. 7.1** Thin film on a thick substrate, irradiated by light under an incidence angle  $\varphi$ . For details see text



is to bring a thin film sample into interaction with electromagnetic radiation. As the result, certain parameters of the electromagnetic radiation will be modified. In spectrophotometry, the focus is on changes in the *intensity* of the light, which is measured and further used to judge on specific sample properties.

This general situation is visualized in Fig. 7.1.

The intensity  $I$  of the light is defined as the amount of light energy penetrating a unit surface area per unit time interval. The *transmittance*  $T$  and *reflectance*  $R$  of the light are defined through the directed transmitted ( $I_T$ ) or specularly reflected ( $I_R$ ) light intensities, divided by the intensity of the incident light ( $I_E$ ):

$$\begin{aligned} T &\equiv \frac{I_T}{I_E} \\ R &\equiv \frac{I_R}{I_E} \end{aligned} \quad (7.1)$$

As soon as the thin film (system) has been prepared on a transparent substrate, the spectrally resolved measurement of  $T$  and  $R$  (at any chosen incidence angle  $\varphi$  and any required polarization state of the incident light) appears as a widely used straightforward characterization tool. Alternatively, spectrally resolved ellipsometric measurements become more and more frequently used in coating characterization practice (compare Chap. 9).

The measurement of both  $T$  and  $R$  under identical conditions provides information on the optical loss  $L$ , which is composed from total scatter  $TS$  and absorptance  $A$ . As a result of energy conservation we have:

$$1 - T - R = L = TS + A \quad (7.2)$$

## 7.2 Theory

### 7.2.1 Basics

As it is evident from Fig. 7.1, a light wave which has penetrated a thin film sample, will carry information about the materials which form the sample (i.e. about both film and substrate material constants), as well as about its geometry (here the thicknesses of film  $h$  and substrate  $h_{sub}$ ). Generally, the same will be true for the reflected wave, because all interfaces can principally contribute to the reflectance spectrum. So that we have to expect, that both  $T$  and  $R$  will be rather complicated functions of all the mentioned construction parameters. Thus, measured  $T$  and  $R$  spectra can be used to gain information about material properties as well as the sample geometry.

In the model case of optically homogeneous, isotropic, and non-magnetic media, the linear optical *material* properties may be expressed in terms of a scalar frequency-dependent complex dielectric function  $\varepsilon(\omega)$  with  $\omega$  - angular frequency of the electromagnetic radiation [1, 2].  $\varepsilon$  is related to the optical constants  $n$  and  $k$  through the relationship:

$$n(\omega) + ik(\omega) = \sqrt{\varepsilon(\omega)} \equiv \hat{n}(\omega) \quad (7.3)$$

Here  $\hat{n}$  is the *complex index of refraction*; its frequency-dependence is called *dispersion*. The absorption coefficient  $\alpha$  is defined as:

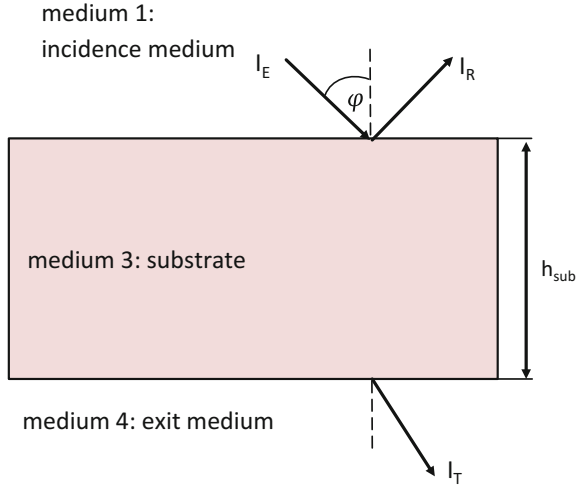
$$\alpha(\omega) = 2 \frac{\omega}{c} k(\omega) \quad (7.4)$$

Let us also mention that a positive imaginary part of the dielectric function results in energy dissipation within a medium. Whenever the dielectric function is purely real, no energy will be dissipated [3].

For characterization purposes, thin films are usually deposited on a much thicker substrate with smooth and parallel surfaces. Therefore, it makes sense to discuss the simplest case of the optical properties of an uncoated substrate first. So we start our discussion from a simplified system like it is shown in Fig. 7.2.

It is rather straightforward to write down the equations for  $T$  and  $R$  of a bare thick substrate. In accordance to Figs. 7.1 and 7.2, let the incidence medium be numbered as medium 1, while the substrate defines medium 3 ( $\hat{n}_3 = \hat{n}_{sub}$  - see Fig. 7.1). Let us further assume, that the incidence (medium 1) and exit media (medium 4) are identical ( $n_4 = n_1$ ). This results in [2]:

Fig. 7.2 Uncoated substrate



$$\begin{aligned}
 T_{calc} &= \frac{|t_{13}|^2 |t_{31}|^2 e^{-4\pi v h_{sub}} \operatorname{Im} \sqrt{\hat{n}_{sub}^2 - n_1^2} \sin^2 \varphi}{1 - |r_{31}|^4 e^{-8\pi v h_{sub}} \operatorname{Im} \sqrt{\hat{n}_{sub}^2 - n_1^2} \sin^2 \varphi} \\
 R_{calc} &= |r_{13}|^2 + \frac{|t_{13}|^2 |r_{31}|^2 |t_{31}|^2 e^{-8\pi v h_{sub}} \operatorname{Im} \sqrt{\hat{n}_{sub}^2 - n_1^2} \sin^2 \varphi}{1 - |r_{31}|^4 e^{-8\pi v h_{sub}} \operatorname{Im} \sqrt{\hat{n}_{sub}^2 - n_1^2} \sin^2 \varphi} \\
 v &\equiv \frac{\omega}{2\pi c} = \lambda^{-1}
 \end{aligned} \tag{7.5}$$

Here, symbols of the type  $t_{ij}$  and  $r_{ij}$  represent nothing else than the Fresnel coefficients for the transmitted and reflected electric field strength at the interface between the  $i$ th and  $j$ th media, respectively [1, 2].  $\omega$  is the angular frequency. Note that at oblique incidence, the Fresnel coefficients are sensitive to the polarization state of the incident light.

Equation (7.5) allow calculating transmittance and reflectance of an uncoated substrate (i.e. a thick slab as shown in Fig. 11.3), taking all internal multiple reflections into account, as well as possible absorption and any effects arising from oblique incidence. Note that (7.5) are obtained when assuming incoherent superposition of all multiple internally reflected wave trains. It cannot be applied to the analysis of thin films, because the latter are usually thin enough to guarantee coherent superposition of internally reflected wave trains.

In the case of normal incidence, (7.5) can be written as:

$$\begin{aligned}
 T_{calc}|_{\varphi=0} &= \frac{(1 - R_{13})^2 e^{-\alpha_{sub} h_{sub}}}{1 - R_{13}^2 e^{-2\alpha_{sub} h_{sub}}} \\
 R_{calc}|_{\varphi=0} &= \frac{R_{13} [1 - e^{-2\alpha_{sub} h_{sub}} (2R_{13} - 1)]}{1 - R_{13}^2 e^{-2\alpha_{sub} h_{sub}}}
 \end{aligned} \tag{7.6}$$

**Table 7.1** Overview on substrate materials, often used for film characterization purposes

Material	Approximate wavelength range of transparency (nm)	Refractive index
Crystalline Germanium Ge	>2000	$n_{sub} \approx 4.0$ (infrared)
Crystalline Silicon Si	>1000	$n_{sub} \approx 3.45$ (infrared)
BK7, B270	350–4500	$n_{sub} \approx 1.52$ (visible)
Fused silica SiO <sub>2</sub>	200–4500	$n_{sub} \approx 1.45$ (visible)
Crystalline Calcium fluoride CaF <sub>2</sub>	130–12000	$n_{sub} \approx 1.43$ (visible)
Crystalline Magnesium fluoride MgF <sub>2</sub>	115–7500	$n_{sub} \approx 1.38$ (visible)

Here  $R_{13}$  denotes the normal incidence intensity reflectance of a single substrate interface:

$$R_{13} = R_{31} = |r_{13}|^2 \quad (7.7)$$

When damping is absent, or even at moderate damping levels, both transmittance and reflectance may be measured and subsequently used for substrate optical characterization. For strong damping, from (7.5) we obtain:

$$\alpha_{sub} h_{sub} \rightarrow \infty : T_{calc} \rightarrow 0; R_{calc} \rightarrow R_{13} \quad (7.8)$$

In this case, substrate transmission is completely suppressed, while we still have a reflection signal, originating from the first substrate surface. The latter still contains all information about the substrate optical constants and may therefore be used for substrate optical characterization as well. Nevertheless, in thin film spectrophotometric characterization, it is most convenient to make use of at least semi-transparent substrates, in order to have both transmission and reflection signals available. Often used substrate materials are summarized in Table 7.1.

## 7.2.2 *Elaboration of Film Thickness and Optical Constants from Single Thin Film Spectra*

### 7.2.2.1 **Basic Equations for Transmittance and Reflectance of a Single Thin Film on a Thick Substrate**

It is now rather straightforward to write down the equations for  $T$  and  $R$  of a single thin film on a thick substrate. Let the film be composed from medium 2, and the substrate from medium 3 ( $\hat{n}_3 = \hat{n}_{sub}$  – see Fig. 7.1). Assuming  $n_4 = n_1$ , in analogy to Sect. 7.2.1, we can write [2]:

$$\begin{aligned}
T_{calc} &= \frac{|t_{123}|^2 |t_{31}|^2 e^{-4\pi v h_{sub} I m \sqrt{\hat{n}_{sub}^2 - n_1^2 \sin^2 \varphi}}}{1 - |r_{321}|^2 |r_{31}|^2 e^{-8\pi v h_{sub} I m \sqrt{\hat{n}_{sub}^2 - n_1^2 \sin^2 \varphi}}} \\
R_{calc} &= |r_{123}|^2 + \frac{|t_{123}|^2 |r_{31}|^2 |t_{321}|^2 e^{-8\pi v h_{sub} I m \sqrt{\hat{n}_{sub}^2 - n_1^2 \sin^2 \varphi}}}{1 - |r_{321}|^2 |r_{31}|^2 e^{-8\pi v h_{sub} I m \sqrt{\hat{n}_{sub}^2 - n_1^2 \sin^2 \varphi}}} \quad (7.9)
\end{aligned}$$

Moreover, we have [1, 2]:

$$\begin{aligned}
t_{ijk} &= \frac{t_{ij} t_{jk} e^{i\delta}}{1 + r_{ij} r_{jk} e^{2i\delta}} \\
r_{ijk} &= \frac{r_{ij} + r_{jk} e^{2i\delta}}{1 + r_{ij} r_{jk} e^{2i\delta}} \quad (7.10)
\end{aligned}$$

Thereby, the superposition of internally reflected light portions within the film is assumed to be completely coherent. The possibly complex phase  $\delta$  is essential for the description of the thin film interference pattern, it is given by [2]:

$$\delta = \frac{\omega}{c} h \sqrt{\hat{n}_2^2 - n_1^2 \sin^2 \varphi} = 2\pi v h \sqrt{\hat{n}_2^2 - n_1^2 \sin^2 \varphi} \quad (7.11)$$

Note that for  $h \rightarrow 0$ ,  $T$  and  $R$  approach the corresponding values of the uncoated substrate, hence the spectrophotometric characterization of ultrathin films ( $h \ll \lambda$ ) is much more complicated than in the case  $h \approx \lambda$  (see next section). In such cases, a spectroellipsometric characterization or even a combination of both approaches may be clearly of use.

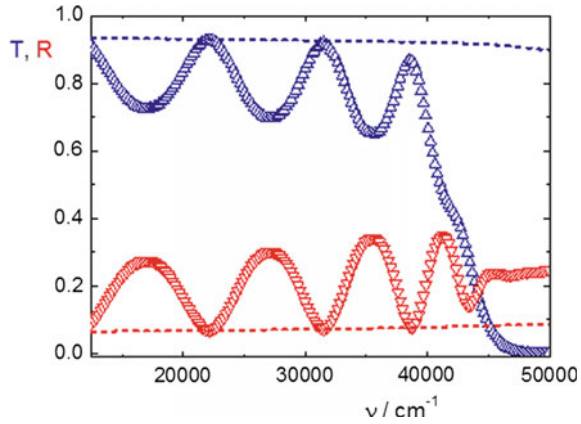
### 7.2.2.2 Information from the Interference Pattern Observed from Dielectric Films

In the case of dielectric or even semiconducting thin films, the couple of (7.9)–(7.11) describes a type of spectra as shown in Fig. 7.3. This figure shows measured spectra of a 211 nm thick zirconium dioxide (zirconia) single film on a fused silica substrate with a thickness of 1 mm. For comparison, the corresponding spectra of the bare (uncoated) substrate are also shown as dashed lines. This is a rather typical thin film spectrum, and it is worth mentioning some of its specific features:

The spectrum may generally be subdivided into several sections, according to the value of the optical loss  $L$  as defined in (7.2).

- In the wavenumber region between  $10000 \text{ cm}^{-1}$  and approximately  $35000 \text{ cm}^{-1}$ , the spectrum appears almost free of optical losses, because  $T$  and  $R$  sum up to 1 in terms of the spectrophotometric measurement accuracy (compare later Sect. 8.1). Hence, the dielectric functions of both film and substrate materials are practically real.

**Fig. 7.3** symbols: normal incidence  $T$ - and  $R$ -spectra of a zirconium oxide thin film on a thick fused silica substrate in the NIR/VIS/UV spectral regions; dashed lines:  $T$  and  $R$  of the bare substrate



- In such spectral regions, dielectric or semiconductor films of suitable thickness usually show a pronounced interference pattern, which may be identified as a series of subsequent maxima and minima in  $T$  and  $R$ , observed at discrete wavenumbers  $\nu_j$ . Certain extrema appear tangential to the bare substrate spectrum; they define what we will call the halfwave (HW) points of the spectrum. The other extrema define quarterwave (QW) points. For normal incidence, the wavenumbers of the extrema are defined by:

$$\begin{aligned}
 \text{QW - points: } n_2 h &= j \frac{\lambda_j}{4}; j = 1, 3, 5 \dots \\
 \text{HW - points: } n_2 h &= j \frac{\lambda_j}{4}; j = 0, 2, 4, \dots \\
 \nu_j &\equiv \frac{1}{\lambda_j}
 \end{aligned} \tag{7.12}$$

- In the case that the QW transmittance appears to be higher than that of the bare substrate (the QW reflectance lower than that of the substrate), the refractive index of the film will be in-between those of the substrate and the ambient. In the practically relevant case, that the ambient medium is air, and the substrate index  $n_{sub} > 1$ , we can conclude that the film index is certainly lower than that of the substrate:  $n_{sub} > n > 1$  (low index coating).
- In the opposite case (as it is relevant for the example shown in Fig. 7.3), the film refractive index is outside the interval spanned by the substrate and ambient indices. In the practically relevant case, that the ambient medium is air, and the substrate index  $n_{sub} > 1$ , we can conclude that the film index is certainly higher than that of the substrate (high index coating).
- The dependence of the QW transmittance/reflectance on the refractive indices  $n$  and  $n_{sub}$  offers the principle possibility for determining the film refractive index by inverting (7.9)–(7.11), independently from knowledge of the film thickness.

On the contrary, when neglecting dispersion, the film thickness may be subsequently estimated from (7.13):

$$h = \frac{1}{4n_2 (v_{j+1} - v_j)} \quad (7.13)$$

- This type of approach may be extended to the analysis of weakly absorbing films, and is in the basis of the so-called *envelope methods* for film characterization [4, 5]. Note that here knowledge about  $n_{sub}$  is usually presumed.
- At oblique incidence, according to (7.11), the interference pattern shifts towards higher wavenumbers (smaller wavelengths). This so-called angular shift offers an alternative method for estimating the film refractive index. Let us assume, that at an angle of incidence  $\varphi_a$ , an interference extremum of arbitrary order  $j$  is observed at the wavelength  $\lambda_a$ . At another angle  $\varphi_b$ , the same interference extremum will have shifted to the wavelength  $\lambda_b$ . When neglecting dispersion, from (7.11) we find:

$$n_2 = n_1 \sqrt{\frac{\lambda_b^2 \sin^2 \varphi_a - \lambda_a^2 \sin^2 \varphi_b}{\lambda_b^2 - \lambda_a^2}} \quad (7.14)$$

Note that this approach does not presume knowledge about  $n_{sub}$ .

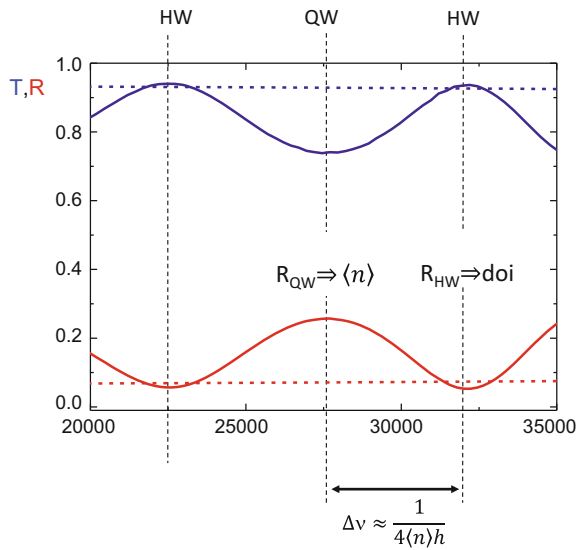
The mentioned spectral characteristics may be used for a first “quick-and-dirty” estimation of refractive index and thickness of the coating in spectral regions with negligible damping. For wavenumbers higher than approximately  $35000 \text{ cm}^{-1}$ , the optical loss according to the spectra shown in Fig. 7.3 appears to be no more negligible. In such spectral regions, the above type of discussion is no more applicable in the strong sense.

Consequently, in the special case that normal incidence  $T$  and  $R$  spectra of both the uncoated substrate (Fig. 7.2) and a film-on-substrate system (Fig. 7.1) are available, a simple straightforward optical dielectric thin film characterization may be performed adhering to the following recipe:

- (i) First measure  $T$  and  $R$  of the bare substrate at normal incidence, as well as the substrate thickness  $h_{sub}$ . Then, the optical constants of the substrate may be calculated inverting (7.6) [6]. In the case that the substrate is completely intransparent, the substrate optical constants can still be deduced from the reflectance of the substrate surface (see later Sect. 8.2.2).
- (ii) Measure  $T$  and  $R$  of the film-on-substrate system and calculate  $L$  according to (11.2). Identify spectral regions where  $L$  is negligible (transparency regions).
- (iii) In transparency regions, identify HW and QW points in the interference pattern. From QW points, make clear whether you deal with a high index or a low index coating.
- (iv) In the case that in the HW points, the  $T/R$ -spectra are tangential to those of the substrate, the film may be tackled as a homogeneous film. In this case, calculate



**Fig. 7.4**  $T$ - and  $R$ -spectra of a gradient index film. Full lines show measured spectra of a zirconia sample with a negative refractive index gradient ( $n_2$  decreases with growing distance from the film-substrate interface), dashed lines correspond to the spectra of a bare substrate



the refractive index from the QW points (inverting (7.9)–(7.11)), using substrate data as determined in point  $\nu_j$ . Note that this procedure is ambiguous for a low index coating, so that one has to identify the physically meaningful solution from side information obtained otherwise. Estimate the film thickness from (7.13).

- (v) In the case that  $L \approx 0$  and the  $T/R$ -spectra are *not* tangential to the substrate spectra in the HW points, the film is expected to show a refractive index gradient (inhomogeneous film) [7]. These effects are no more covered by (7.9)–(7.11). In this case, the measured  $T$  and  $R$ -values in the HW points embody important information about the so-called *degree of inhomogeneity* (doi), while the corresponding values in the QW points correspond to an average refractive index  $\langle n \rangle$ , while averaging is performed over the film thickness. So that HW points give information on the doi, while QW points on the average index. This situation is schematically sketched in Fig. 7.4, which shows measured spectra of an inhomogeneous zirconium oxide film. Note that in this particular case, the origin of the refractive index gradient becomes obvious when comparing with the TEM image shown in Fig. 2.2. It stems from a similar sample and confirms a depth-dependent porosity as well as a depth-dependent degree of crystallinity in a real zirconia film, which has a direct impact on the spectrum.
- (vi) Having estimated the film thickness as well as the refractive index in the transparency region, the (averaged over the film thickness) extinction coefficient may be estimated from (7.9)–(7.11) in any spectral region.

### 7.2.2.3 Curve Fit Procedures

A more precise elaboration of film thickness and optical constants is possible in terms of so-called curve fit procedures [8]. In this case, measured (exp) spectral curves are fitted by theoretical (calc) spectra calculated according to (7.9)–(7.11). The sets of optical constants which result in a sufficiently good fit of experimental spectra form a set of possible mathematical solutions to the characterization problem. Once the solution of such fitting attempts is usually ambiguous, side knowledge on the optical constants behavior (compare later Sect. 7.3.1) as well as on the thickness is highly welcome to identify the physically meaningful solution from the set of solutions of the mathematical fitting procedure.

Mathematically, the fit may be performed by minimizing a discrepancy function  $DF$  of the type as defined in (7.15):

$$DF = \sqrt{\frac{1}{N} \sum_{l=1}^N \left\{ [T_{exp}(v_l) - T_{calc}(v_l; \hat{n}(v_l); h)]^2 + [R_{exp}(v_l) - R_{calc}(v_l; \hat{n}(v_l); h)]^2 \right\}} \quad (7.15)$$

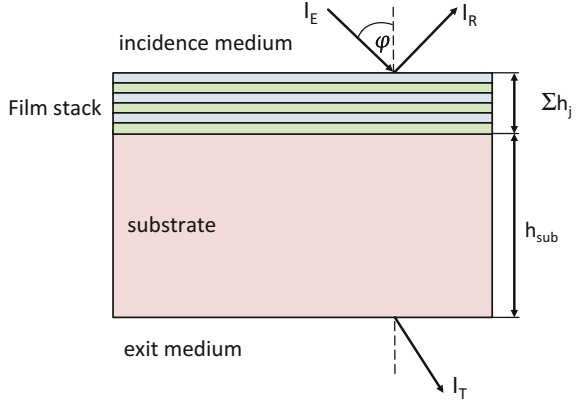
Here, the choice of  $\{v_l\}$  defines a grid of discrete data points which enter into the discrepancy function (7.15) to be minimized (compare later Sect. 8.1.4). Of course, one can include more than two spectra (even including ellipsometric data) into the expression (7.15). The data obtained earlier from the interference pattern (if available) may serve here as a reliable initial approximation for further minimizing (7.15). Examples of curve fits with different degrees of complexity will be presented in Sect. 8.2.3.

### 7.2.3 Multilayer Spectra Evaluation

In the case of multilayer characterization, we have a series of films stacked on the substrate as shown in Fig. 7.5.

Equation (7.9) nevertheless preserve their general structure, although values like  $t_{123}$  and  $r_{123}$  have to be replaced by the more general expressions  $t_{stack}$  and  $r_{stack}$ . Symbols characterizing reverse light propagation direction ( $t_{321}$  and  $r_{321}$ ) have to be replaced by new expressions  $t'_{stack}$  and  $r'_{stack}$ . The new field transmission and reflection coefficients  $t_{stack}$ ,  $r_{stack}$ ,  $t'_{stack}$  and  $r'_{stack}$  may be calculated in terms of the matrix formalism [1, 2]. They carry information about optical constants and thicknesses of all individual layers which compose the film stack shown in Fig. 7.5. Correspondingly, instead of (7.9), we now have the expressions (7.16):

Fig. 7.5 Multilayer system



$$\begin{aligned}
 T_{calc} &= \frac{|t_{stack}(\{\hat{n}_j\}, \{h_j\})|^2 |t_{31}|^2 e^{-4\pi v h_{sub} l m \sqrt{\hat{n}_{sub}^2 - n_1^2 \sin^2 \varphi}}}{1 - |r'_{stack}(\{\hat{n}_j\}, \{h_j\})|^2 |r_{31}|^2 e^{-8\pi v h_{sub} l m \sqrt{\hat{n}_{sub}^2 - n_1^2 \sin^2 \varphi}}} \\
 R_{calc} &= |r_{stack}(\{\hat{n}_j\}, \{h_j\})|^2 \\
 &+ \frac{|t_{stack}(\{\hat{n}_j\}, \{h_j\})|^2 |r_{31}|^2 |t'_{stack}(\{\hat{n}_j\}, \{h_j\})|^2 e^{-8\pi v h_{sub} l m \sqrt{\hat{n}_{sub}^2 - n_1^2 \sin^2 \varphi}}}{1 - |r'_{stack}(\{\hat{n}_j\}, \{h_j\})|^2 |r_{31}|^2 e^{-8\pi v h_{sub} l m \sqrt{\hat{n}_{sub}^2 - n_1^2 \sin^2 \varphi}}}
 \end{aligned}
 \tag{7.16}$$

Here, the individual layers forming the stack are numbered in terms of the subscript  $j$ .

In the case that  $T$  and  $R$  have been measured, a fit of these experimental data may again be performed by minimizing a suitable discrepancy function. Instead of (7.15), one now has to minimize a discrepancy function of the type (7.17):

$$DF = \sqrt{\frac{1}{N} \sum_{l=1}^N \{ [T_{exp}(v_l) - T_{calc}(v_l; \{\hat{n}_j(v_l)\}; \{h_j\})]^2 + [R_{exp}(v_l) - R_{calc}(v_l; \{\hat{n}_j(v_l)\}; \{h_j\})]^2 \}}
 \tag{7.17}$$

When keeping in mind the tremendous number of unknown values  $\{\hat{n}_j(v_l)\}$  and  $\{h_j\}$ , a reliable re-engineering procedure (i.e. determination of the optical constants and the thicknesses from the measured spectra) appears to be a rather hopeless effort. There are two basic approaches to facilitate the situation:

- (a) Reducing the number of parameters to be determined.
- (b) Increasing the number of input data, i.e. measured spectra.

(a): In many situations, optical constants of the materials forming the stack are known with sufficient accuracy. In this case, the re-engineering task reduces to the determination of the set of individual layer thicknesses  $\{h_j\}$ . This may still be difficult enough, but a further reduction of unknown values may be achieved when making use

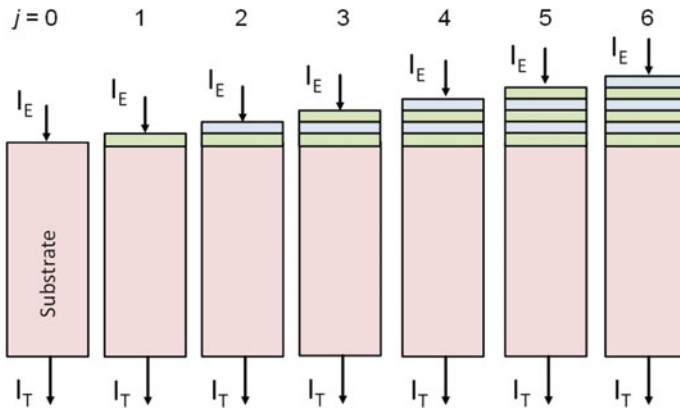


**Fig. 7.6** Principle of acquisition of in situ transmission spectra during multilayer coating deposition

of correlations between individual film thicknesses and/or optical constants, defined by systematic deposition errors inherent to the specific thickness monitoring strategy applied during multilayer deposition [9].

(b): On the other hand, the number of measured data entering into (7.17) may be enhanced.  $T$  and  $R$  measurements may be performed at different angles of incidence, compare later Sect. 3.1. Also, spectroellipsometric data may be included into (7.17) [10].

But the inclusion of more independent ex situ measurement data like oblique incidence spectrophotometry and ellipsometry appears to be both time- and cost consuming because of expansive extra equipment required. An alternative is provided by the use of in situ spectrophotometry (or spectroellipsometry), where numerous experimental data about  $T$  and/or  $R$  measured on the not yet finished stack are collected directly during the film deposition.

The idea is simple (Fig. 7.6). Let us assume that the film deposition chamber is equipped with a spectrophotometer that allows measuring  $T$  and/or  $R$  directly during multilayer coating deposition. This will allow, for example, a spectrum recording immediately after each of the individual layers (numbered by  $j$ ) has been deposited. Typically, a “0th” spectrum is recorded prior to starting deposition, it corresponds to the spectrum of the bare substrate ( $j = 0$ ) and may be used for calibration purposes. Then, the 1st spectrum is recorded after the first layer has been deposited ( $j = 1$ ). It contains information about the optical constants and thickness of the first layer. Then, deposition proceeds with the second layer, again followed by a spectra recording. That second spectrum contains information about optical constants and thicknesses of two layers, and so on. Finally, we will obtain as many spectra as there are individual layers in the stack. This is a tremendous amount of information, and it is obtained from one single spectrometer set-up, which can operate automatically without any additional sample handling. Moreover, when fast spectrometers are used, the amount of extra time necessary for spectra recording during coating deposition is of no relevance.

When fitting in situ spectra one must keep in mind, that optical constants (and even layer thicknesses) in a coating may principally change when the coating is exposed to air and heated up or cooled down to its operation temperature. Therefore, one has to distinguish between in situ and ex situ optical constants. This is particularly relevant for porous coatings, prepared in vacuum conditions by PVD techniques. We will not discuss all the corresponding models here (some simple considerations will be made in Sect. 7.3.3, compare also Sect. 2.3). Instead, we will assume that the in situ relevant optical constants are well-known, and the only task of in situ spectroscopy is the reliable determination of the individual layer thicknesses. This task may be solved by means of a so-called full triangular re-engineering algorithm [11]. In the following we will give a short explanation of this algorithm. The basic principle is visualized in Fig. 7.6. The superscript “ $T$ ” indicates spectra used in the triangular algorithm.

Let us assume that a first transmission spectrum  $T_{meas}^{T(1)}(\nu_l)$  is recorded when the first layer has been deposited. This spectrum depends only on the thickness of the first layer  $h_1$ . The second spectrum  $T_{meas}^{T(2)}(\nu_l)$  is recorded after the deposition of the second layer has been completed. It naturally depends on two thickness values  $h_1$  and  $h_2$ . This process is repeated until the full multilayer coating deposition has finished. The essence of the full triangular re-engineering algorithm is to determine all thickness values simultaneously by fitting all those transmission spectra by the corresponding theoretical spectra  $T_{calc}^{T(j)}(\nu_l)$ . Thickness calculation is thus achieved by minimizing the *triangular discrepancy function*  $DF^T$  [11]:

$$DF^T(h_1, \dots, h_J) = \left[ \frac{1}{JN} \sum_{j=1}^J \sum_{l=1}^N \left( \frac{T_{meas}^{T(j)}(\nu_l) - T_{calc}^{T(j)}(\nu_l, h_1, \dots, h_j)}{\Delta T^T(\nu_l)} \right)^2 \right]^{\frac{1}{2}} \quad (7.18)$$

Here  $J$  is the number of individual layers deposited at the relevant state of the deposition process.  $\Delta T^T(\nu_l)$  is the in situ transmittance measurement error.

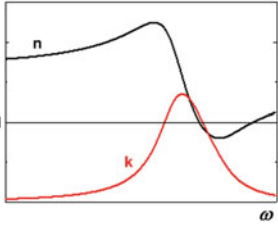
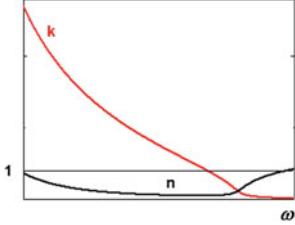
So far, in situ spectroscopy combined with the full triangular algorithm is accepted to be the most reliable tool for individual layer thickness determination in complicated optical coatings. For different application examples see references [12–14].

## 7.3 Further Information Gained from Optical Constants

### 7.3.1 Basic Classical Dispersion Models and Analytic Properties of the Dielectric Function

As already mentioned, the dielectric function, and consequently the optical constants, appear to be frequency-dependent. This phenomenon is called dispersion. For selected material systems, this frequency dependence may be reliably modelled in

**Table 7.2** Optical constants in terms of the oscillator and Drude dispersion models

Bound charge carriers: Lorentzian Single Oscillator model Application: bound electrons in dielectrics and metals	Free charge Carriers: Drude Model Application: Free electrons in metals
$\frac{\epsilon(\omega)-1}{\epsilon(\omega)+2} = \frac{\hat{n}^2-1}{\hat{n}^2+2} = \frac{N_{bound}}{3} \frac{q^2}{\epsilon_0 m} \frac{1}{\omega_0^2 - \omega^2 - 2i\omega\gamma}$	$\epsilon(\omega) = 1 - \frac{\omega_p^2}{\omega^2 + 2i\gamma\omega}; \quad \omega_p = \sqrt{\frac{N_{free}q^2}{\epsilon_0 m}}$
$N_{bound}$ : concentration of bound charge carriers $m$ : mass of bound charge carriers $q$ : their charge $\omega_0$ : their resonance frequency $\gamma$ : damping constant	$N_{free}$ : concentration of free charge carriers $m$ : mass of free charge carriers $q$ : their charge $\gamma$ : damping constant
	

terms of rather compact dispersion models. The Lorentzian oscillator model as well as the Drude model can be regarded as the basic classical dispersion models for the description of optical properties of dielectrics and metals [1, 2, 15]. Their main features are summarized in Table 7.2.

When looking on the picture in the left column of Table 7.2, the most striking feature in the optical response of a system with bound charge carriers is *resonance behavior* of the extinction coefficient at  $\omega \rightarrow \omega_0$ , which results in rather strong damping of the propagating wave. Note that apart from resonance (transparency region), the refractive index increases with increasing frequency, which is called *normal dispersion*. Close to resonance (strong damping), the refractive index decreases with increasing frequency (*anomalous dispersion*).

This type of dispersion is in strong contrast to that described by the Drude model (right column of Table 7.2). Here the refractive index may be significantly smaller than the extinction coefficient as long as the light frequency is well below the plasma frequency. Such a behaviour of the optical constants results in high reflection at the air-material-interface, as it is typically observed at metal surfaces. When describing the optical behavior of metals in terms of the Drude model, parameters like the concentration of free electrons become accessible as well as derived parameters such like dc conductivity  $\sigma_{stat}$  ( $\sigma_{stat} = \epsilon_0 \omega_p^2 / (2\gamma)$ ) and the damping constants or relaxation times corresponding to the free electrons motion [2].

In rather transparent dielectrics, as a rule, from Table 7.2 we observe that the condition  $k \ll n$  is fulfilled. Good metals, i.e. metals where the optical response is dominated by the free electron fraction, show the opposite behavior, namely  $k \gg n$ .

The obviously correlated behaviour of  $n$  and  $k$  as visualized in the Table 7.2 can be tackled as the manifestation of a more general relation between the real and imaginary parts of the dielectric function as expressed in terms of the Kramers–Kronig relations [16]:

$$\begin{aligned} \operatorname{Re} \varepsilon(\omega) &= 1 + \frac{2}{\pi} VP \int_0^{\infty} \frac{\operatorname{Im} \varepsilon(\xi) \xi d\xi}{\xi^2 - \omega^2} \\ \operatorname{Im} \varepsilon(\omega) &= -\frac{2\omega}{\pi} VP \int_0^{\infty} \frac{[\operatorname{Re} \varepsilon(\xi) - 1]}{\xi^2 - \omega^2} d\xi + \frac{\sigma_{stat}}{\varepsilon_0 \omega} \end{aligned} \quad (7.19)$$

VP denotes the Cauchy principal value of the integral. (7.19) is in consistency with the relations:

$$\operatorname{Re} \varepsilon(\omega) = \operatorname{Re} \varepsilon(-\omega); \quad -\operatorname{Im} \varepsilon(\omega) = \operatorname{Im} \varepsilon(-\omega) \quad (7.20)$$

It is easily checked, that the dispersion relations given in Table 7.2 are consistent with these fundamental requirements.

Analogous relations may also be formulated for the optical constants [17]. Here we have for insulators as well as conductors:

$$\begin{aligned} n(\omega) &= 1 + \frac{2}{\pi} VP \int_0^{\infty} \frac{k(\xi) \xi d\xi}{\xi^2 - \omega^2} \\ k(\omega) &= -\frac{2\omega}{\pi} VP \int_0^{\infty} \frac{[n(\xi) - 1]}{\xi^2 - \omega^2} d\xi \end{aligned} \quad (7.21)$$

Kramers–Kronig-consistency is a strong and useful criterion for the physical relevance of any dispersion law used in coating characterization or design practice.

As a direct consequence from (7.19), the following useful relationships are obtained:

Static dielectric constant of a dielectric:

$$\varepsilon_{stat} = \varepsilon(\omega = 0) = 1 + \frac{2}{\pi} \int_0^{\infty} \frac{\operatorname{Im} \varepsilon(\omega)}{\omega} d\omega \quad (7.22)$$

The static dielectric constant of a dielectric is thus always larger than 1.

In the *high frequency limit*, contrarily, we find (convergence supposed):

$$\operatorname{Re} \varepsilon(\omega) = 1 + \frac{2}{\pi} VP \int_0^{\infty} \frac{\operatorname{Im} \varepsilon(\xi) \xi d\xi}{\xi^2 - \omega^2} \Bigg|_{\omega \rightarrow \infty} \rightarrow 1 - \frac{2}{\pi \omega^2} \int_0^{\infty} \operatorname{Im} \varepsilon(\xi) \xi d\xi < 1 \quad (7.23)$$

As a rule, in the extreme ultraviolet (EUV) or soft X-ray spectral ranges, the dielectric function as well as the refractive index are therefore smaller than but close to 1.

An utmost important sum rule interconnects the full concentration of oscillators  $N$  (i.e. oscillating electrons on the background of heavy nuclei) with the integral energy dissipation:

$$N = \frac{2\varepsilon_0 m}{\pi q^2} \int_0^{\infty} \operatorname{Im} \varepsilon(\omega) \omega d\omega \quad (7.24)$$

Rewriting (7.24) in terms of the optical constants – see (7.3) and (7.4), one immediately obtains:

$$N = \frac{2\varepsilon_0 m c}{\pi q^2} \int_0^{\infty} n(\omega) \alpha(\omega) d\omega \quad (7.25)$$

Here we arrive at the fundament of any quantitative spectrophotometric analysis, where the concentration of any kind of absorption centres (molecules, impurities, and so on) is obtained from the integral over the measured absorbance. Of course, in practice, the integration in (7.25) may be performed only over a finite frequency interval accessible to the measurement.

### 7.3.2 Often Used Other Dispersion Models

Clearly, the mentioned basic models correspond to rather idealized situations, and in characterization practice, more complicated dispersion models have to be applied. In our treatment, we will restrict on models relevant for description of optical properties from the middle infrared up to the ultraviolet spectral regions. This way we include models relevant for infrared analytics (atomic nuclei vibrations), rather transparent materials for interference coating applications, modelling the absorption edge(s) in (selectively) absorbing materials for light blocking, optoelectronics, and solar energy conversion, as well as metals for reflector optics or light blocking purposes. A schematic overview on optical constants and single film optical behavior of typical dielectric, semiconductor and transparent conductive oxide (TCO) materials from the infrared up to the ultraviolet is presented in Fig. 7.7.

As it is shown in Fig. 7.7, many dielectric or semiconducting materials offer a broad transparency range, which usually extends from the near infrared to the



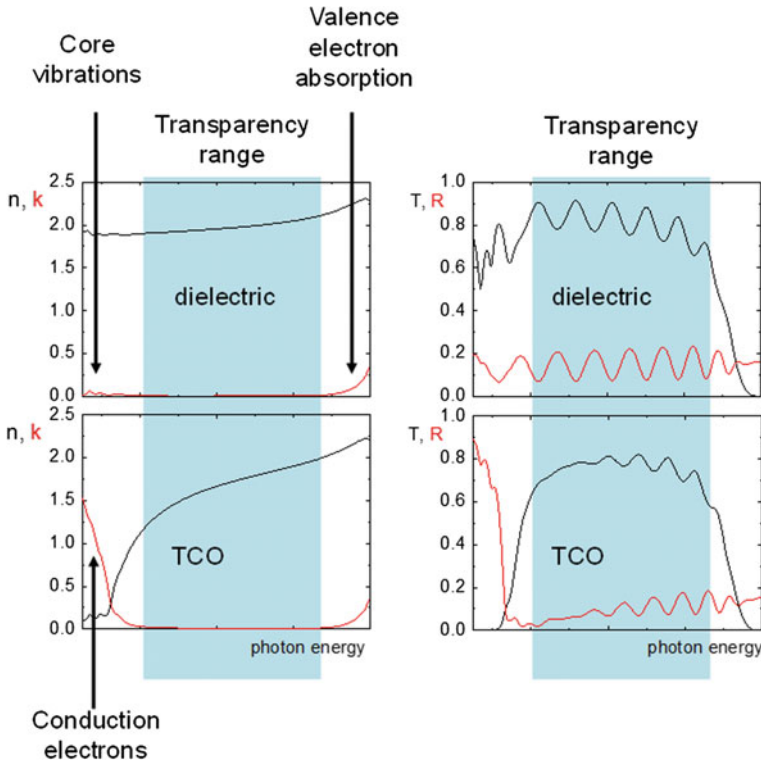


**Fig. 7.7** Transparency range in dielectric/undoped semiconducting (on top) or transparent conductive oxide (TCO) materials (on bottom). The photon energy is given by  $\hbar\omega$

visible or even the ultraviolet spectral ranges. At the short wavelength (high photon energy) side, transparency is limited by the onset of valence electron excitations, which marks the energy position of the fundamental absorption edge. At the long wavelength (low photon energy) side, it is limited by optical excitation of atomic nuclei vibrations, which occur in the middle infrared spectral range. However, in TCO materials, optical excitation of free electron movement may result in additional transparency range shrinking at low photon energies.

Some often used dispersion models useful for describing properties of dielectrics, metals, and semiconductors from the infrared to the ultraviolet spectral ranges are summarized in Table 7.3.

**Table 7.3** Selected dispersion models. Symbols according to [15],  $f$  denotes the oscillator strength

Model	Equation	Application/remarks
Lorentzian Multi-oscillator	$\varepsilon(\omega) = 1 + \sum_j \frac{f_j}{\omega_{0j}^2 - \omega^2 - 2i\omega\gamma_j}$	Superposition of Lorentzian oscillators with different resonance frequencies; good for fitting spectra of dielectrics and semiconductors with complicated absorption shapes
Merger of Drude- and multioscillator	$\varepsilon(\omega) = 1 - \frac{\omega_p^2}{\omega^2 + 2i\gamma\omega} + \sum_j \frac{f_j}{\omega_{0j}^2 - \omega^2 - 2i\omega\gamma_j}$	Superimposes contributions of free and bound charge carriers, good for describing optical properties of any electrically conducting materials, including TCOs
Brendel model [18]	$\varepsilon(\omega) = 1 + \frac{1}{\sqrt{2\pi}\sigma} \int_{-\infty}^{\infty} \exp\left[-\frac{(\xi - \omega_0)^2}{2\sigma^2}\right] \frac{f}{\xi^2 - \omega^2 - 2i\gamma\omega} d\xi$	Particular case of the multioscillator model; describes inhomogeneously broadened (with respect to a Gaussian statistics) absorption lines. Describes Lorentzian, Gaussian, and Voigt line shapes
Tauc-Lorentz model [19]	$Im \varepsilon(\omega) = \frac{const.}{\omega} \frac{\gamma(\omega - \omega_{gap})^2}{(\omega_0^2 - \omega^2)^2 + 4\gamma^2\omega^2}; \omega \geq \omega_{gap}$ $Im \varepsilon(\omega) = 0; \omega < \omega_{gap}$	Merger of the Tauc power law [20] dependence of the absorption coefficient with a Lorentzian. Often used for amorphous semiconductors in the vicinity of the fundamental absorption edge. The real part of $\varepsilon$ may be calculated in terms of (7.19). The optical Tauc gap is given by $\hbar\omega_{gap}$
Cody-Lorentz model [21]	$Im \varepsilon(\omega) = const. \frac{\omega}{(\omega - \omega_{gap})^2 + \omega_0^2} \frac{\gamma(\omega - \omega_{gap})^2}{(\omega_0^2 - \omega^2)^2 + 4\gamma^2\omega^2}; \omega > \omega_1$ $Im \varepsilon(\omega) = \frac{\omega_1}{\omega} \exp\left[\frac{\omega - \omega_1}{\omega_0}\right]; 0 < \omega \leq \omega_1$	Merger of the Cody power law [21] dependence of the absorption coefficient with a Lorentzian and an Urbach tail [22]. Often used for amorphous semiconductors in the vicinity of the fundamental absorption edge. The real part of $\varepsilon$ may be calculated in terms of (7.19). The optical Cody gap is given by $\hbar\omega_{gap}$

### 7.3.3 Optical Properties of Material Mixtures

Let us now assume a mixture built up from several constituents, numbered by  $j$ . Let us further assume, that we know the optical constants (or the dielectric function  $\varepsilon_j$ ) of any of the constituents. Let it be our task to determine the optical constants of the mixture.

We will make the following assumptions:

Let the mixture occupy the full volume  $V$ . In the mixture, let us assume that each of the constituents occupies a certain volume fraction  $V_j$ . The corresponding volume filling factor  $p_j$  of the  $j$ th material in the mixture is then defined as:

$$p_j \equiv \frac{V_j}{V} \quad (7.26)$$

Obviously,

$$\sum_j p_j = 1 \quad (7.27)$$

Traditionally, the mixing partners are tackled as small (compared to the wavelength) inclusions numbered by the subscript  $j$ , embedded in a certain host medium with a dielectric function  $\varepsilon_h$  [23]. This assumption leads to the general mixing formula:

$$\frac{(\varepsilon_{eff} - \varepsilon_h)}{\varepsilon_h + (\varepsilon_{eff} - \varepsilon_h)L} = \sum_j p_j \frac{(\varepsilon_j - \varepsilon_h)}{\varepsilon_h + (\varepsilon_j - \varepsilon_h)L} \quad (7.28)$$

Here  $L$  is the so-called depolarization factor, and  $\varepsilon_{eff}$  is the effective dielectric function of the mixture. Note that  $0 \leq L \leq 1$  holds. In the case of spherical inclusions, set  $L = 1/3$ .

Table 7.4 provides a survey of mixing models that represent special cases of the general formula (7.28).

Knowledge on the optical behavior of mixtures is of extreme practical relevance, because no real material can be regarded as absolutely pure. Contrarily, it may be composed from several crystalline and amorphous phases, it may contain stoichiometric as well as non-stoichiometric fractions as well as several kinds of impurities. Even the zirconia film shown in Fig. 2.2 cannot be regarded as a pure film: It is obviously a mixture of crystalline and amorphous zirconia fractions, and a pore fraction.

In this sense, mixture models even provide a vehicle for understanding the origin of the difference between in situ and ex situ optical constants as mentioned in Sect. 7.2.3. Indeed, when a coating is prepared in vacuum conditions, the pores are empty, and so the pore fraction is characterized by a “pore refractive index” that is equal to 1. At atmosphere, however, water may penetrate into the pores, changing the pore’s refractive index to a value of approximately 1.33. The resulting effects in the optical

**Table 7.4** Survey of mixing models [2]

Model	Equation	Application/remarks
Parallel nanolaminate	$\varepsilon_{eff} = \sum_j p_j \varepsilon_j$	Nanolaminate oriented parallel to the orientation of the electric field vector. Obtained from (7.28) when setting $L = 0$
Vertical nanolaminate	$\varepsilon_{eff}^{-1} = \sum_j p_j \varepsilon_j^{-1}$	Nanolaminate oriented vertical to the orientation of the electric field vector. Obtained from (7.28) when setting $L = 1$
Maxwell Garnett	$\frac{(\varepsilon_{eff} - \varepsilon_l)}{\varepsilon_l + (\varepsilon_{eff} - \varepsilon_l)L} = \sum_{j \neq l} p_j \frac{(\varepsilon_j - \varepsilon_l)}{\varepsilon_l + (\varepsilon_j - \varepsilon_l)L}$	Guest-host system with the $l$ th mixing partner acting as the host. Obtained from (7.28) when setting $\varepsilon_h = \varepsilon_l$
Lorentz-Lorenz	$\frac{(\varepsilon_{eff} - 1)}{1 + (\varepsilon_{eff} - 1)L} = \sum_j p_j \frac{(\varepsilon_j - 1)}{1 + (\varepsilon_j - 1)L}$	Guest-host system with vacuum acting as the host. Obtained from (7.28) when setting $\varepsilon_h = 1$
Bruggeman	$0 = \sum_j p_j \frac{(\varepsilon_j - \varepsilon_{eff})}{\varepsilon_{eff} + (\varepsilon_j - \varepsilon_{eff})L}$	Molecular mixtures, obtained from (7.28) when setting $\varepsilon_h = \varepsilon_{eff}$ . Also known as effective medium approximation (EMT or EMA)

properties of the coating may be calculated in terms of suitable mixing models and are known as the vacuum-to-air shift [15] (compare also Chap. 2, Sect. 2.3).

### 7.3.4 An Empirical Extension of the Multi-oscillator Model: The Beta Distributed Oscillator ( $\beta_{do}$ ) Model

As it is indicated in Fig. 7.7, in a limited spectral range, the merger of the Drude and Lorentzian multioscillator model is well suited for describing the dielectric function of a large variety of materials. When the spectral range includes the fundamental absorption edge, the required number of Lorentzian oscillators for accurate modelling the dielectric function increases and the resulting large number of parameters often results in numerical instabilities in the fitting process. A reduction of the required number of parameters could be achieved when a suitable distribution function for the oscillator's strength is used. A prominent example is the Brendel model (Table 7.3), which makes use of a Gaussian distribution of resonance frequencies. Another promising approach is given by the Beta distribution:

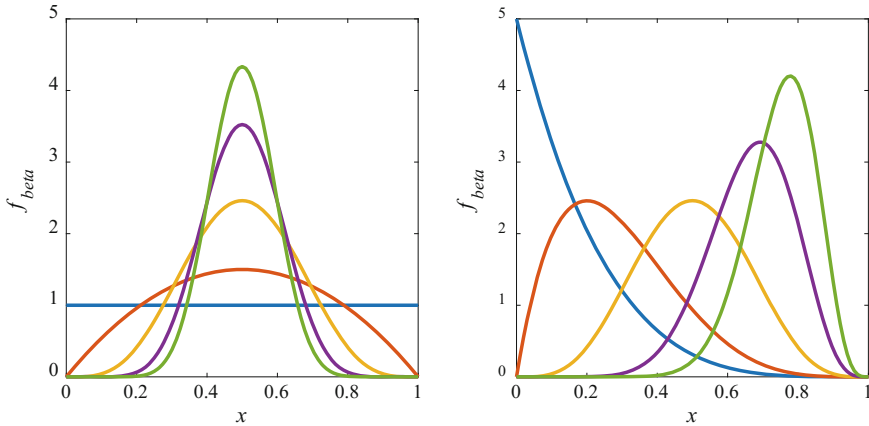


**Fig. 7.8** Probability density functions of the beta distribution (left:  $\alpha = \beta$ , right:  $\beta = 5$ , blue:  $\alpha = 1$ , red:  $\alpha = 2$ , yellow:  $\alpha = 5$ , violet:  $\alpha = 10$ , green:  $\alpha = 15$ )

$$f_{beta}(x, \alpha, \beta) = \frac{\Gamma(\alpha+\beta)}{\Gamma(\alpha)\Gamma(\beta)} x^{\alpha-1} (1-x)^{\beta-1} = \frac{x^{\alpha-1}(1-x)^{\beta-1}}{B(\alpha, \beta)} \text{ for } 0 \leq x \leq 1 \tag{7.29}$$

$$f_{beta}(x, \alpha, \beta) = 0 \text{ for } x < 0 \text{ or } x > 1$$

where  $\Gamma(z)$  is the gamma function and  $B(\alpha, \beta)$  is the beta function, defined by:

$$B(\alpha, \beta) = \int_0^1 x^{\alpha-1} (1-x)^{\beta-1} dx \tag{7.30}$$

The beta function can be easily generalized to cover an arbitrary interval  $[v_{min}, v_{max}]$ :

$$f_{beta}(\xi, \alpha, \beta, v_{min}, v_{max}) = \frac{(\xi - v_{min})^{\alpha-1} (v_{max} - \xi)^{\beta-1}}{B(\alpha, \beta) (v_{max} - v_{min})^{\alpha+\beta-1}} \tag{7.31}$$

When  $\alpha = \beta$  the distribution will be symmetric (Fig. 7.8 left). For  $\alpha = \beta = 1$  a uniform  $[0,1]$  distribution and for  $\alpha = \beta \rightarrow \infty$  a delta function at the midpoint can be generated. In the case  $\alpha \neq \beta$  the distribution function will be skewed (Fig. 7.8 right).

For practical application of the beta distribution for modelling the oscillator strength distribution in optical materials a further property seems prospective. Even the case of normally distributed oscillator strength (Brendel model) can be approximated quite well by a symmetric beta distribution. In Fig. 7.9 the (truncated) normal distribution with mean value 0.5 and standard deviation 0.1 is shown (circle). The shape is very close to a beta distribution with  $\alpha = \beta = 13$  (solid line).

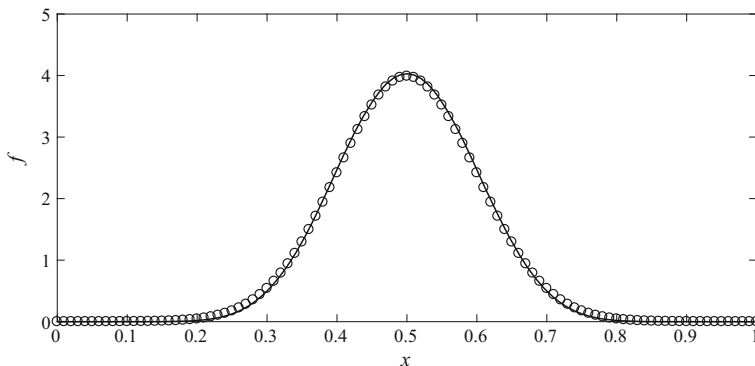


**Fig. 7.9** Probability density functions of the normal distribution (circle, mean: 0.5, standard deviation: 0.1) and beta distribution (solid line,  $\alpha = \beta = 13$ )

To apply the beta distribution to the Lorentzian multi oscillator model the dependence of the susceptibility  $\hat{\chi}_j(\nu)$  of a  $j$ th single oscillator from wavenumber  $\nu$  can be used (compare Table 7.3):

$$\hat{\chi}_j(\nu) = \frac{f_j}{\tilde{\nu}_{0j}^2 - \nu^2 - 2i\nu\Gamma_j} \quad (7.32)$$

For compatibility reasons to the current implementation of the oscillator model used in LCalc software [24], a slightly different formulation will be used:

$$\hat{\chi}_j(\nu) = \frac{J_j}{\pi} \left( \frac{1}{\nu_{0j} - \nu - i\Gamma_j} + \frac{1}{\nu_{0j} + \nu + i\Gamma_j} \right) \quad (7.33)$$

Let us introduce the complex function  $X(\xi, \nu)$ . It is defined according to:

$$X(\xi, \nu) = \frac{J_{beta,j}}{\pi} \left( \frac{1}{\xi - \nu - i\Gamma_{beta,j}} + \frac{1}{\xi + \nu + i\Gamma_{beta,j}} \right) \quad (7.34)$$

To replace the  $j$ th single oscillator by a set of beta distributed oscillators located in the interval  $[\nu_{min,j}, \nu_{max,j}]$ , we write:

$$\hat{\chi}_{beta,j}(\nu) = \int_{\nu_{min,j}}^{\nu_{max,j}} f_{beta}(\xi, \alpha_j, \beta_j, \nu_{min,j}, \nu_{max,j}) X(\xi, \nu) d\xi \quad (7.35)$$

Instead of the single Lorentzian line, as defined by the imaginary part of (7.32), expression (7.35) describes an inhomogeneously broadened absorption structure, which might be used for modelling the absorption edge shape in thin solid films.

Next, the integral function will be replaced by a finite sum. Thereby, an equidistant grid of  $N$  wavenumbers can be used

$$\nu_{s,j} = \nu_{min,j} + s \cdot \Delta\xi \text{ with } s \in [1, N] \text{ and } \Delta\xi = \frac{\nu_{max,j} - \nu_{min,j}}{N + 1} \quad (7.36)$$

Then, the susceptibility of the set of beta distributed oscillators (“ $\beta\_do$ ”) can be calculated by

$$\begin{aligned} \hat{\chi}_{beta,j}(\nu) &= \sum_{s=1}^N f_{beta}(\nu_{s,j}, \alpha, \beta, \nu_{min,j}, \nu_{max,j}) X(\nu_{s,j}, \nu) \Delta\xi \\ &= \frac{1}{(N + 1) B(\alpha, \beta)} \sum_{s=1}^N \frac{(\nu_{s,j} - \nu_{min,j})^{\alpha-1} (\nu_{max,j} - \nu_{s,j})^{\beta-1}}{(\nu_{max,j} - \nu_{min,j})^{\alpha+\beta-2}} X(\nu_{s,j}, \nu) \end{aligned} \quad (7.37)$$

Additionally, it is convenient to replace the beta function also by a sum (compare (7.30)):

$$B(\alpha, \beta) = \frac{1}{N + 1} \sum_{s=1}^N \frac{(\nu_{s,j} - \nu_{min,j})^{\alpha-1} (\nu_{max,j} - \nu_{s,j})^{\beta-1}}{(\nu_{max,j} - \nu_{min,j})^{\alpha+\beta-2}} \quad (7.38)$$

From (7.31), (7.33)–(7.35), the susceptibility can be calculated by:

$$\hat{\chi}_{beta,j}(\nu) = \frac{\sum_{s=1}^N w_{s,j} \frac{J_{beta,j}}{\pi} \left( \frac{1}{\nu_{s,j} - \nu - i\Gamma_{beta,j}} + \frac{1}{\nu_{s,j} + \nu + i\Gamma_{beta,j}} \right)}{\sum_{s=1}^N w_{s,j}} \quad (7.39)$$

with weight factors

$$w_{s,j} = \frac{(\nu_{s,j} - \nu_{min,j})^{\alpha_j-1} (\nu_{max,j} - \nu_{s,j})^{\beta_j-1}}{(\nu_{max,j} - \nu_{min,j})^{\alpha_j+\beta_j-2}} = \left( \frac{s}{N + 1} \right)^{\alpha_j-1} \left( \frac{N + 1 - s}{N + 1} \right)^{\beta_j-1} \quad (7.40)$$

Equations (7.39) and (7.40) essentially define what we will further call the beta distributed oscillator model ( $\beta\_do$  model). In Fig. 7.10 the individual contributions from a beta distributed oscillator set to real and imaginary part of the susceptibility are shown.

The impact of the line width to real and imaginary part of susceptibility for a beta distributed set of oscillators is shown in Fig. 7.11. In trend, the width of the imaginary part of the susceptibility decreases with the line width of the underlying individual oscillators. When the line width becomes small in comparison to the width of the beta distribution, the resulting shape becomes dominated by the beta distribution.

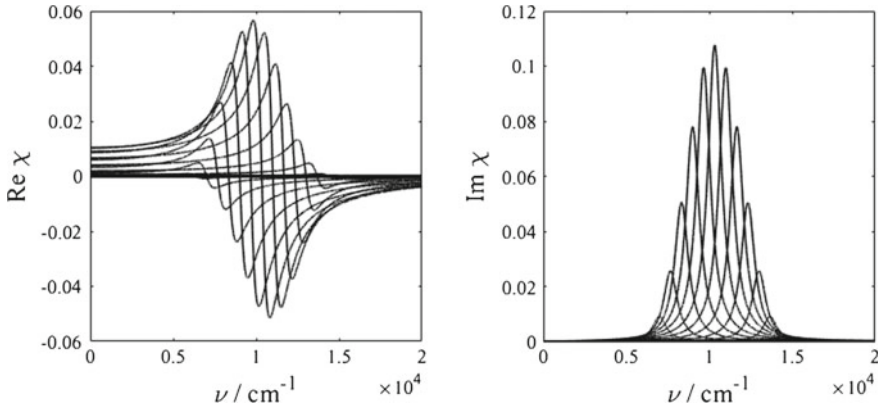


**Fig. 7.10** Real (left) and imaginary part (right) of susceptibility of individual equally spaced Lorentzian oscillators defined by the  $\beta\_do$  model ( $N = 15$ ,  $\nu_{min} = 5000 \text{ cm}^{-1}$ ,  $\nu_{max} = 15000 \text{ cm}^{-1}$ ,  $J_{beta} = 1000 \text{ cm}^{-1}$ ,  $\Gamma_{beta} = 500 \text{ cm}^{-1}$ ,  $\alpha = \beta = 5$ )

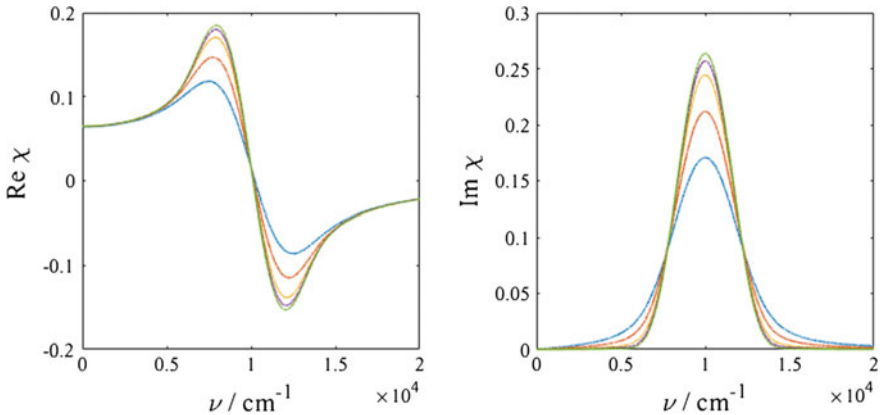


**Fig. 7.11** Real (left) and imaginary part (right) of the susceptibility in the  $\beta\_do$  model ( $N = 1000$ ,  $\nu_{min} = 5000 \text{ cm}^{-1}$ ,  $\nu_{max} = 15000 \text{ cm}^{-1}$ ,  $J_{beta} = 1000 \text{ cm}^{-1}$ , blue:  $\Gamma_{beta} = 1000 \text{ cm}^{-1}$ , red:  $\Gamma_{beta} = 500 \text{ cm}^{-1}$ , yellow:  $\Gamma_{beta} = 200 \text{ cm}^{-1}$ , violet:  $\Gamma_{beta} = 100 \text{ cm}^{-1}$ , green:  $\Gamma_{beta} = 50 \text{ cm}^{-1}$ )

### 7.4 Conclusions

In this chapter, basic theoretical concepts and equations necessary for spectrophotometric characterization of thin films and film systems have been introduced. Particularly the  $\beta\_do$  model turns out to be extremely useful in coating characterization practice, including typical inorganic dielectric coatings, but also metal coatings, semiconductor films, and even organic molecular films. In Chap. 8, corresponding examples will be presented and discussed.



## References

1. M. Born, E. Wolf, *Principles of Optics* (Pergamon Press, Oxford, 1968)
2. O. Stenzel, *The Physics of Thin Film Optical Spectra: An Introduction*. Springer Series in Surface Sciences, vol. 44, 2nd edn. (Springer, Berlin, 2015)
3. R. Gross, A. Marx, *Festkörperphysik* (Walter de Gruyter GmbH, Berlin, 2014)
4. J.C. Manificier, J. Gasiot, J.P. Fillard, A simple method for the determination of the optical constants  $n$ ,  $k$  and the thickness of a weakly absorbing thin film. *J. Phys. E: Sci. Instrum.* **9**, 1002–1004 (1976)
5. I. Ohlidal, K. Navrátil, Simple method of spectroscopic reflectometry for the complete optical analysis of weakly absorbing thin films: application to silicon films. *Thin Solid Films* **156**, 181–190 (1988)
6. E. Nichelatti, Complex refractive index of a slab from reflectance and transmittance: analytical solution. *J. Opt. A: Pure Appl. Opt.* **4**, 400–403 (2002)
7. A.V. Tikhonravov, M.K. Trubetskov, B.T. Sullivan, J.A. Dobrowolski, Influence of small inhomogeneities on the spectral characteristics of single thin films. *Appl. Opt.* **36**, 7188–7198 (1997)
8. J.H. Dobrowolski, F.C. Ho, A. Waldorf, Determination of optical constants of thin film coating materials based on inverse synthesis. *Appl. Opt.* **22**, 3191–3200 (1983)
9. T.V. Amotchkina, M.K. Trubetskov, V. Pervak, B. Romanov, A.V. Tikhonravov, On the reliability of reverse engineering results. *Appl. Opt.* **51**, 5543–5551 (2012)
10. V. Janicki, J. Sancho-Parramon, O. Stenzel, M. Lappschies, B. Görtz, C. Rickers, C. Polenzky, U. Richter, Optical characterization of hybrid antireflective coatings using spectrophotometric and ellipsometric measurements. *Appl. Opt.* **46**, 6084–6091 (2007)
11. A.V. Tikhonravov, M.K. Trubetskov, On-line characterization and reoptimization of optical coatings. *Proc. SPIE* **5250**, 406–413 (2004)
12. T.V. Amotchkina, M.K. Trubetskov, V. Pervak, S. Schlichting, H. Ehlers, D. Ristau, A.V. Tikhonravov, Comparison of algorithms used for optical characterization of multilayer optical coatings. *Appl. Opt.* **50**, 3389–3395 (2011)
13. S. Wilbrandt, O. Stenzel, N. Kaiser, Experimental determination of the refractive index profile of rugate filters based on in situ measurements of transmission spectra. *J. Phys. D* **40**, 1435–1441 (2007)
14. S. Wilbrandt, O. Stenzel, M. Bischoff, N. Kaiser, Combined in situ and ex situ optical data analysis of magnesium fluoride coatings deposited by plasma ion assisted deposition. *Appl. Opt.* **50**, C5–C10 (2011)
15. O. Stenzel, *Optical Coatings: “Material Aspects in Theory and Practice”* (Springer, Berlin, 2014)
16. L.D. Landau, E.M. Lifschitz, *Lehrbuch der theoretischen Physik, Bd. VIII: Elektrodynamik der Kontinua* [engl.: Textbook of Theoretical Physics, Vol. VIII: Electrodynamics of Continuous Media] (Akademie, Berlin, 1985)
17. V. Lucarini, J.J. Saarinen, K.E. Peiponen, E.M. Vartiainen, *Kramers-Kronig relations in Optical Materials Research* (Springer, Berlin, 2005)
18. R. Brendel, D. Bormann, An infrared dielectric function model for amorphous solids. *J. Appl. Phys.* **71**, 1–6 (1992)
19. G.E. Jellison, Spectroscopic ellipsometry data analysis: measured versus calculated quantities. *Thin Solid Films* **313**(314), 33–39 (1998)

20. J. Tauc, R. Grigorovic, A. Vancu, Optical properties and electronic structure of amorphous germanium. *Phys. Stat. Sol.* **15**, 627–637 (1966)
21. A.S. Ferlauto, G.M. Ferreira, J.M. Pearce, C.R. Wronski, R.W. Collins, X. Deng, G. Ganguly, Analytical model for the optical functions of amorphous semiconductors from the near-infrared to ultraviolet: applications in thin film photovoltaics. *J. Appl. Phys.* **92**, 2424–2436 (2002)
22. F. Urbach, The long-wavelength edge of photographic sensitivity and of the electronic absorption of solids. *Phys. Rev.* **92**, 1324 (1953)
23. D.E. Aspnes, J.B. Theeten, F. Hottier, Investigation of effective-medium models of microscopic surface roughness by spectroscopic ellipsometry. *Phys. Rev. B* **20**, 3292–3302 (1979)
24. O. Stenzel, S. Wilbrandt, K. Friedrich, N. Kaiser, Realistische Modellierung der NIR/VIS/UV-optischen Konstanten dünner optischer Schichten im Rahmen des Oszillatormodells. *Vak. Forsch. Prax.* **21**(5), 15–23 (2009)